Journal of ELECTRONIC MATERIALS, Vol. 47, No. 8, 2018
https://doi.org/10.1007/s11664-018-6352-0

Effect of Annealing on the Density of Defects in Epitaxial CdTe (211)/GaAs

EMINE BAKALI ,[1,2] YUSUF SELAMET,[1] and ENVER TARHAN[1]

1.—Department of Physics, Izmir Institute of Technology, 35430 Urla, Izmir, Turkey. 2.—e-mail: eminebakali@gmail.com

CdTe thin films were grown on GaAs (211) wafers by molecular beam epitaxy as the buffer layer for HgCdTe infrared detector applications. We studied the effect of annealing on the density of dislocation of these CdTe thin films under varying annealing parameters such as annealing temperature, annealing duration, and number of cycles. Annealings were carried out using a home-made annealing reactor possessing a special heater element made of a Si wafer for rapid heating. The density of dislocations, which were made observable with a scanning electron microscope after etching with an Everson solution, were calculated by counting the number of dislocations per unit surface area, hence the term etch pit density (EPD). We were able to decrease EPD values by one order of magnitude after annealing. For example, the best EPD value after a 20-min annealing at 400°C was $\sim 2 \times 10^7$ cm^{-2} for a 1.63-μm CdTe thin film which was about 9.5×10^7 cm^{-2} before annealing. We also employed Raman scattering measurements to see the changes in the structural quality of the samples. From the Raman measurements, we were able to see improvements in the quality of our samples from the annealing by studying the ratio of 2LO/LO phonon mode Raman intensities. We also observed a clear decrease in the intensity of Te precipitations-related modes, indicating a decrease in the size and number of these precipitations.

Key words: Cadmium telluride, Thermal cycle annealing, EPD, Dislocations, MBE, Raman spectroscopy

INTRODUCTION

HgCdTe (mercury cadmium telluride, MCT) is the most common material for infrared (IR) detectors spanning from the very long wavelength to the short wavelength region of the electromagnetic spectrum. This was achieved by growing MCT materials with varying Hg-Cd concentrations. The band gap of $Hg_{1-x}Cd_xTe$ varies with x ($0 \le x \le 1$). For $x = 0$, HgTe is a negative band gap semiconductor which is a semimetal with no optical gap. As Cd concentration increases, the negative gap shrinks and becomes zero at $x = 0.14$. When $x > 0.14$, the optical gap opens and widens almost linearly, and with increasing Cd concentration x, reaches 1.5 eV at room temperature for $x = 1$ which is the band gap energy of CdTe.[1] The superior detector performance of MCT is due to its high electron mobility. For example, at 80 K, the electron mobility of $Hg_{0.8}Cd_{0.2}Te$ can be as high as a few hundred thousand cm^2/(V s),[2] while that of Si is only about 2,000 cm^2/(V s) at 80 K.[3] Even though some mid-wavelength IR (MWIR) detectors such as InSb and InAs perform better, MCT is the only detector material covering the widest range from 20 μm (VLWIR; very long wavelength IR) to 2 μm (SWIR; short wavelength IR) with a very high performance close to those of InAs and InSb in the MWIR region.[4]

Thin film MCTs are grown mainly on one of the three fundamental alternative substrates, namely: CdZnTe (CZT), Si, and GaAs.[5,6] MCT films grown on lattice-matched CZT substrates exhibit the lowest etch pit density (EPD; an indication of surface

(Received December 4, 2017; accepted May 3, 2018; published online May 21, 2018)

dislocation density; see the "Experimental" section) value of 8×10^4 cm^{-2}, but they have more micro-defects (micrometer-sized large defects) compared to those grown on both Si and GaAs substrates.[7,8] In addition, CZT has other drawbacks such as high cost, fragility, and availability in mostly small sizes. In contrast, Si and GaAs substrates have the advantage of being cheaper, more durable, and more abundant than CZT, but they are lattice mismatched with MCT and require a buffer layer for strain relaxation to reduce defects in the MCTs. The lowest EPD values obtained on such substrates are about 10^6 cm^{-2} which is almost two orders of magnitude higher than those grown on CdZnTe. In this study, we chose GaAs as the substrate material mainly because it has better lattice and thermal matches with MCT compared to those of Si, while it also has better physical properties than those of CZT.

High dislocation density values of MCT and large (greater than a few percent) thermal mismatches between MCT and the substrate greatly reduce the detector performance.[9] The lattice mismatch between the substrate and MCT is the main cause of dislocations in MCT films. The reduction of dislocations is usually achieved by using a proper lattice-matched buffer layer between the substrate and the MCT film.[6,10] In that respect, CdTe is the most preferred buffer layer material in terms of its very small lattice and thermal mismatch percentages, which are less than 1% and 1.85%, respectively.[11]

When a buffer layer, such as CdTe, is used, most of the dislocations in MCT originate from this layer. Hence, a reduction of dislocations in the buffer layer causes a reduction in the defect densities in MCT, increasing its detector performance. Annealing as a post-growth treatment is a common choice of method for the reduction of dislocations in the buffer layer prior to the growth of MCT on it. The effect of annealing has been studied by different groups for CdTe[12] and MCT.[13–16]

In this work, we studied the reduction of the density of dislocation defects in CdTe/GaAs thin films using post-growth annealing methods. The reduction of dislocations during an annealing procedure stems from two simultaneous but alternative dislocation reactions, which are annihilation or coalescence reactions given by the processes[17];

$$D_1 \xrightarrow{K_1} \text{annihilation}; \tag{1}$$

$$D_1 + D_1 \xrightarrow{K_2} D_2, \quad \text{coalescence}, \tag{2}$$

where D_1 and D_2 are the density of dislocations and coalesced dislocations, respectively, and K_1 and K_2 are rate constants of annihilation and coalescence, respectively. Reaction equations are:

$$\frac{dD_1}{dt} = -K_1 D_1 - K_2 D_1^2, \tag{3}$$

$$\frac{dD_2}{dt} = n\frac{K_2 D_1^2}{2}, \tag{4}$$

where n is the fraction of dislocations (D_1) which is less than 1/2. Taking D_0 as the initial value of D_1 at $t = 0$, and assuming initially that here are no coalesced dislocations, that is, $D_2 = 0$ at $t = 0$, the solutions of Eqs. 3 and 4 give the dislocation densities as a function of time:

$$D_1 = \left\{ -\left(\frac{K_2}{K_1}\right) + \left[\left(\frac{1}{D_0} + \frac{K_2}{K_1}\right)\right] e^{K_1 t} \right\}^{-1}, \tag{5}$$

$$D_2 = \left(D_0^2 n \frac{K_2}{K_1}\right)\left\{1 - \left[e^{-K_1 t}\right]^2\right\}. \tag{6}$$

According to Ref. 18, coalescence is the dominant process for defect reduction during annealing, especially for CdTe, Si and GaAs materials. Thus, one can ignore annihilation rate K_1 compared to K_2. Then, the solution for the EPD becomes;

$$D_1 = \frac{D_0}{1 + D_0 K_2 t}. \tag{7}$$

The coalescence parameter K_2 depends on the velocity v of dislocations as[18]

$$K_2 = Av, \tag{8}$$

where A is an empirical constant. The velocity of a dislocation at a temperature T is given as:

$$v = v_0 e^{-\frac{Q}{kT}} \tag{9}$$

where Q is the activation energy of a dislocation motion, k the Boltzmann constant and T the temperature. Here, v_0 corresponds to dislocation velocities at very high temperatures.

We employed two methods to monitor the improvements in the sample quality with varying annealing parameters. The first method is called the EPD method after Everson[19] which is used for the calculation of the number of dislocation defects per unit surface area. The second method is the investigation of Raman peak intensity ratios of longitudinal optical (LO) and second-order longitudinal optical (2LO) phonon modes which indicate the structural quality of our samples.

Raman scattering has been used as an essential spectroscopic tool to identify the electronic, vibrational, and rotational energy levels of atoms, molecules, or condensed matter in all forms since the Raman effect was discovered in 1928.[20] A. Mooradian and G.B. Wright were the first to see LO and TO (transverse optical) phonon modes in CdTe with Raman scattering in 1968.[21] In addition to the investigation of bulk material properties, such as phonon modes, electronic transitions, etc., Raman spectroscopy can also be employed to study

defects in the host material, since many defects produce Raman active modes. By studying intensities, shifts in the peak positions, and line shapes in the Raman spectra of such defects, one can obtain information about their nature.[22]

Among many growth issues, Te precipitation formations in CdTe films play a major role in the degradation of their qualities.[23] The first identification of Raman peaks of Te precipitations in CdTe crystals grown by the Bridgeman method was by Shin et al. in 1983.[23] In 1984, Amirtharaj et al.[24] analyzed the 141-cm^{-1} band and discovered that this band was a combination of E (Te) and TO (CdTe) modes. According to Williams and Vere,[25] Te point defects, formed during a bulk MCT growth, have high mobilities and will form clusters during cooling after a high-temperature growth. Chew et al. identified Te precipitates on the surfaces of MBE-grown CdTe films from their diffraction patterns obtained from a transmission electron microscope, and concluded that they were formed at low temperatures due to second phase breakdown.[26]

Overtones of LO phonon modes of CdTe, i.e., 2LO, 3LO, 4LO, 5LO, and 6LO, were observed for the first time in 1989 from a few-microns-thick CdTe samples excited by laser lines ranging from 457.94 nm to 514.54 nm.[27] Feng et al. used a 488-nm excitation line, and the ratio of the intensity of the Raman bands measured at 80 K for the 2LO mode to that of the LO mode (the 2LO/LO bands intensity ratio) was found to be 0.92. Other overtones bands have also been identified with varying excitation lines.[28] For example, in Contreras et al., the 2TO mode observed at 275 cm^{-1} with an 830-nm excitation line shows a 2TO/LO bands intensity ratio of 1/50.

EXPERIMENTAL

In this work, CdTe buffer layers were grown on (211) GaAs wafers in a molecular beam epitaxy (MBE) (VEECO GEN 20)[29] chamber. Two Epi-ready GaAs wafers were bought commercially from AXT.[30] The first wafer was a disk with a 4 in. (c.10 cm) diameter and the second wafer was a quarter of a disk with a 3 in. (c.7.5 cm) diameter (in a pie shape). Before growth, the oxide capping layer of the GaAs wafers was removed by heating it at 830°C for 6 min and at 715°C for 18 min for the first and the second wafers, respectively, under As overpressure. By observing the development of the expected diffraction pattern from the RHEED port of the MBE growth chamber, we were convinced that the oxide layer was removed for both wafers. Then, an initiation layer was grown at 380°C for 30 s. Next, the growth temperature was set to 600°C for the first and 450°C for the second wafer. All temperatures indicated so far were measured with a thermocouple. Under a specific choice of growth parameters, such as target temperature, effusion cell shutter aperture, etc., the growth rate was usually about 1 μm/h. After the growth of the CdTe films on the GaAs substrates, the first wafer had a 1.63-μm-thick CdTe layer and was named as CT9, while the second wafer had a 5.05-μm-thick CdTe layer which was named as CT10. Samples from the CT9 and CT10 wafers were cut as squares of a few mm length on each side. Thus, we obtained two groups of samples for both the CT9 and CT10 wafers. Next, the CT9 and CT10 samples were annealed under a certain set of parameters for each sample. We monitored the changes in the sample qualities and surface dislocation densities as a function of the annealing parameters.

Our homemade annealing system (Fig. 1a) consists of a sample heater block placed in the middle of a sealed quartz tube of 60 cm length and 2 in. (c.5 cm) diameter. The heater block is made of two stainless steel electrodes with a standard size n-type Si wafer (100) connecting them. The annealing of a sample was carried out by first placing it on the Si wafer which was then heated via a current through it under low pressure (a few Pa). The annealing temperature was adjusted by changing the heating current. According to Laake et al.,[31] when a current is increased suddenly from zero to a set value, the temperature of the heating Si wafer also increases sharply and reaches a maximum value asymptotically in several seconds with no overshooting.

The heater temperature (T) versus current (I) calibration was carried out by separately melting each of four different chunks of materials which consisted of 'pure' In, Se, Zn, and Al elements. Their melting points are 156.6°C, 217°C, 419.58°C, and 660.37°C, respectively.

The annealing of the CT9 and CT10 samples were carried out by placing them on the heater in the middle of the quartz tube in the annealing set-up. The tube was first evacuated down to a few Pa pressure for efficient annealing, then it was purged with Ar gas for a few minutes and pumped again. This process was repeated 10 times to obtain a clean environment for annealing. The heater temperature was kept constant for a certain annealing duration. Cycle annealing was carried out by heating a sample rapidly up to a set annealing temperature at which the sample was annealed for a fixed duration, then the heater current was turned off and the sample was naturally cooled for 15 min in each cycle. This process was repeated for a number of cycles. The total annealing time was calculated as the number of cycles multiplied by the annealing duration of each cycle.

In this study, we investigated the effects of annealing parameters such as annealing temperature, annealing time, and cycle number on the structural qualities of the CT9 and CT10 samples using resonant Raman spectroscopy and x-ray diffractometry (XRD). Then, the Everson etch decoration method, the details of which are given below, was used for the calculation of dislocation densities.

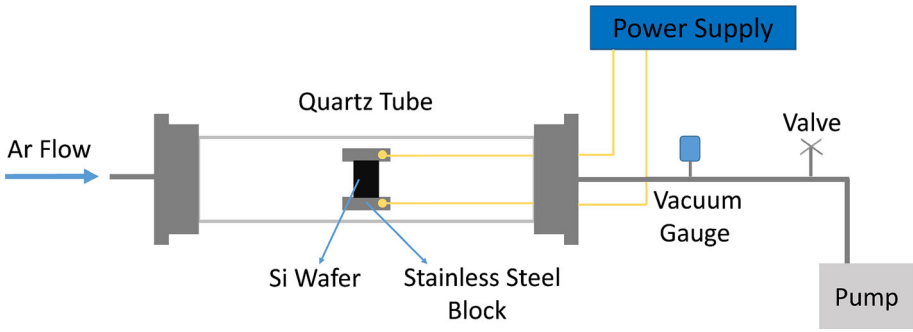

Fig. 1. The annealing set-up with a sample heater in quartz tubing.

Raman measurements were carried out using an S&I Mono Vista Raman System[32] at six different temperatures ranging from room temperature (RT) down to 80 K in a Linkam cooling chamber (THMS600E).[33] The Raman system consists of an Ar-Ion laser with 488- and 514-nm excitation lines which are directed onto a sample placed under the objective of an upright Olympus BX51 microscope. Scattered light collected by the objective is sent to a Princeton Instruments monochromator (ACTON SP2750) with a 750-mm focal length and a set of three gratings (150, 600, and 1800 grooves/mm). The spectrum is then collected by a charge-coupled device (CCD) detector to be sent to the main controlling computer as digital data for analysis. We used the 488-nm excitation line of the Ar laser for all Raman measurements, since CdTe exhibits a good resonance effect because the incident photon energy with this wavelength, being nearly equal to the energy separation between the Γ_7 split-off valence band and the Γ_6 conduction band (resonant Raman scattering). To judge the quality of our samples, we compared the Raman intensity ratio of the 2LO mode to that of the LO mode peaks (bands) which was given as 0.92 for the 488-nm excitation line measured at 80 K.[27] We used this value as a reference for an "ideal sample" since it is the only value given in the literature for a 'good CdTe film'.

To calculate the dislocation densities on the sample surfaces, an Everson etch solution was used for the decoration of dislocations after the XRD and Raman analyses. The etching solution consisted of 25 ml lactic acid, 4 ml nitric acid, and 1 ml hydrofluoric acid. The samples were etched at RT by immersing them and shaking them gently in the solution for an etch duration of about 15 s. The etched samples were rinsed with deionized water, then dried with nitrogen gas. Afterwards, the samples were scanned by scanning electron microscope (SEM) and the dislocation densities were calculated by counting the number of etch pits per unit sample surface area (defined as etch pit density; EPD) from the SEM micrographs of the samples.[34]

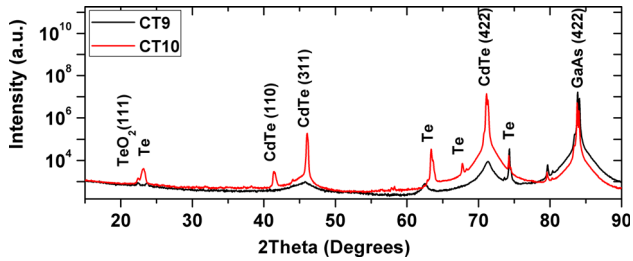

Fig. 2. XRD data of the CT9 and CT10 samples.

RESULTS AND DISCUSSION

In Fig. 2, we can see the XRD spectra of the as-grown CT9 and CT10 wafers before they were cut into several pieces. The peaks at 2θ = 41°, 46°, and 71° are due to CdTe (110), (311), and (422) planes, respectively.[35] Peaks at 22°, 23°, 63°, 67°, and 74° are Te-related peaks[36] whose existence has already been reported by Chew et al. in MBE-grown CdTe films.[26] According to the XRD spectra, the CT10 wafer had more Te precipitation than the CT9 wafer, as inferred from their relative Te-related peak intensities with respect to those of the CdTe-related peaks. The XRD spectrum of CT10 also exhibits additional CdTe (311) and (110) peaks which are almost unobservable in the XRD spectrum of the CT9 wafer.

Figure 3 shows a typical Raman spectrum of a CdTe film on a GaAs substrate (CT9-an25, annealed at 420°C for 5 min) measured at 200 K. The CdTe LA, LO, and 2LO phonon modes are seen at 105 cm^{-1}, 166 cm^{-1}, and 334 cm^{-1}, respectively. The E_1, A_1, and E_2 peaks are due to the corresponding vibrational modes of the Te precipitates in CdTe.[22,24,26,27,37–44] The existence of Te-related Raman peaks confirms the interpretation of the Te peaks in the XRD data. The peak labeled as 1 at 76 cm^{-1} is possibly due to an optical phonon transition from the zone center to the A_2 symmetry point, while the peak 2 at 84 cm^{-1} may be due to a combination of optical phonon transitions from the zone center to the Γ_2 and M_2 points in the Brillioin zone of Te.[43] Peaks 3 and 4 are also phonon peaks, possibly due to transitions from the zone center to

other critical points in the first phonon Brilloin zone of Te. In the same figure, the calculated curve was obtained by fitting all the experimental peak positions to proper Lorentz functions. Since we do not see any GaAs-related phonon peaks in the Raman spectra of all the samples we measured, we can conclude that either the laser light does not reach the GaAs substrate and is totally absorbed by CdTe films or a very small portion of it reaches the GaAs but the Raman scattered light from GaAs is too weak to be observed in the spectra.

Raman spectra of the CT9 and CT10 wafers (before annealing) and the CT9-AN20 (annealed at 375°C for 5 min) and CT10-AN46 (annealed at 400°C for 5 min) samples are illustrated in Fig. 4 (all of our annealed samples were named with an AN prefix with a number). Each figure shows a series of Raman spectra of a sample where each spectrum was measured at a different temperature ranging from 80 K to 296 K. After carrying out a background subtraction, each peak intensity value was normalized to that of the LO peak (hence the nomenclature; "normalized intensity"). We notice that, in all cases, the intensity of the 2LO peak increases from 80 K to 150 K, then gradually decreases and becomes almost zero at 296 K. Table I gives the calculated 2LO to LO peak intensity ratios. We infer from Fig. 4 and Table I that the probability of the annihilation or creation of two LO phonons simultaneously increases as the temperature increases from 80 K to 150 K, while it decreases when the temperature increases from 150 K to 296 K. Also, the intensities of the Te peaks (especially A_1 and E_2) increase with increasing measurement temperature due to increasing number of Te phonons with temperature. Thus, we conclude that the structural quality of CdTe films can be assessed with Raman spectroscopy by studying the intensity ratios of the 2LO to LO peaks at low temperatures, specifically at 80 K, while the measurements at higher temperatures, especially at room temperature (296 K), give information about the Te precipitates.

Raman spectra of the CT9 and CT10 samples, annealed at 400°C, taken at 80 K are given in Fig. 5. We notice that the A_1 and E_2 peaks almost disappear after a 20-min annealing which indicates a decrease in the Te precipitation amounts in these

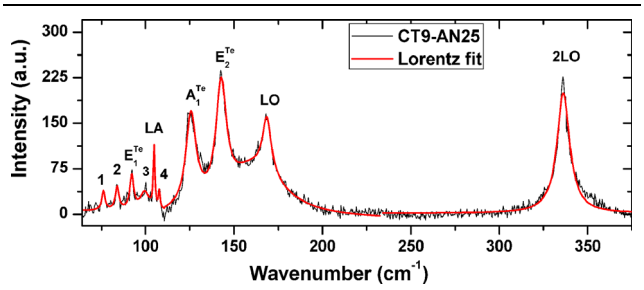

Fig. 3. Raman spectrum of the CT9-AN25 at 200 K.

samples. Figure 6 gives the intensity ratios of the Te A_1 peaks to the CdTe LO mode peaks for the CT9 samples plotted as a function of annealing temperature in (a), annealing time in (b), and the same intensity ratios are plotted for CT10 samples at 400°C annealing temperature with changing annealing times in (c). Each curve with a different data point shape represents a different measurement temperature. According to Fig. 6a, the I_{A_1}/I_{LO} intensity ratio reaches a minimum at about 400°C, then increases slightly. Thus, we conclude that 400°C is the ideal annealing temperature for the CT9 samples. From Fig. 6b, it is seen that, for the CT9 samples annealed at the same temperature with different annealing durations, at about 5 min annealing duration the I_{A_1}/I_{LO} ratio reaches a minimum, then remains steady. Therefore, 5 min is an adequate duration for the annealing of these samples at 400°C. Figure 6c shows the change in the I_{A_1}/I_{LO} ratio for varying annealing durations for the CT10 samples annealed at 400°C. From the figure, it is clear that about 10 min annealing duration is sufficient for the I_{A_1}/I_{LO} ratio to reach a minimum, indicating the maximum reduction in the amount of Te precipitates which increases the quality of the CdTe samples.[40]

Intensity ratios of the peaks observed at 144 cm^{-1} (the 144 peak) to the CdTe LO peaks are given in Fig. 7 as a function of annealing temperature and annealing time. There are two possible processes contributing to the 144 peak: it could be a pure Te E_2 transition, a pure CdTe TO transition, or a proper combination of both. From Fig. 7a–c, we see that the intensity ratios for this peak to the LO peak intensities follow those for the Te A_1 peaks to the CdTe LO peaks. Thus, we conclude that the peak at 144 cm^{-1} is mainly due to Te E_2 transitions for both the CT9 and CT10 samples. The rapid reduction of intensities of the Te-related A_1 and E_2 (144 cm^{-1}) peaks in the CT9 samples compared to those in the CT10 samples is consistent with the XRD results, which show that there are more Te-related peaks in the CT10 samples than those in the CT9 samples, indicating that the CT10 samples have higher Te precipitate concentrations than the CT9 samples. Thus, the reduction of Te precipitate concentrations in the CT10 samples takes longer than that in the CT9 samples. In addition, the CT9 samples are thinner, which further speeds up the Te annihilation process.

Intensity ratios of the 2LO to LO phonon modes (I_{2LO}/I_{LO}) of epitaxial CdTe films are expected to be nearly 1 at 80 K for resonant Raman scattering for a good quality CdTe sample.[27] Figure 8 shows the I_{2LO}/I_{LO} ratios for the CT9 samples with increasing annealing temperatures for a 5-min annealing duration for each annealing temperature. The I_{2LO}/I_{LO} ratios for the CT9 samples show a slight and linear decrease in their Raman spectra for all Raman temperatures except for 296 K, for which there was no noticeable 2LO peak. We also notice

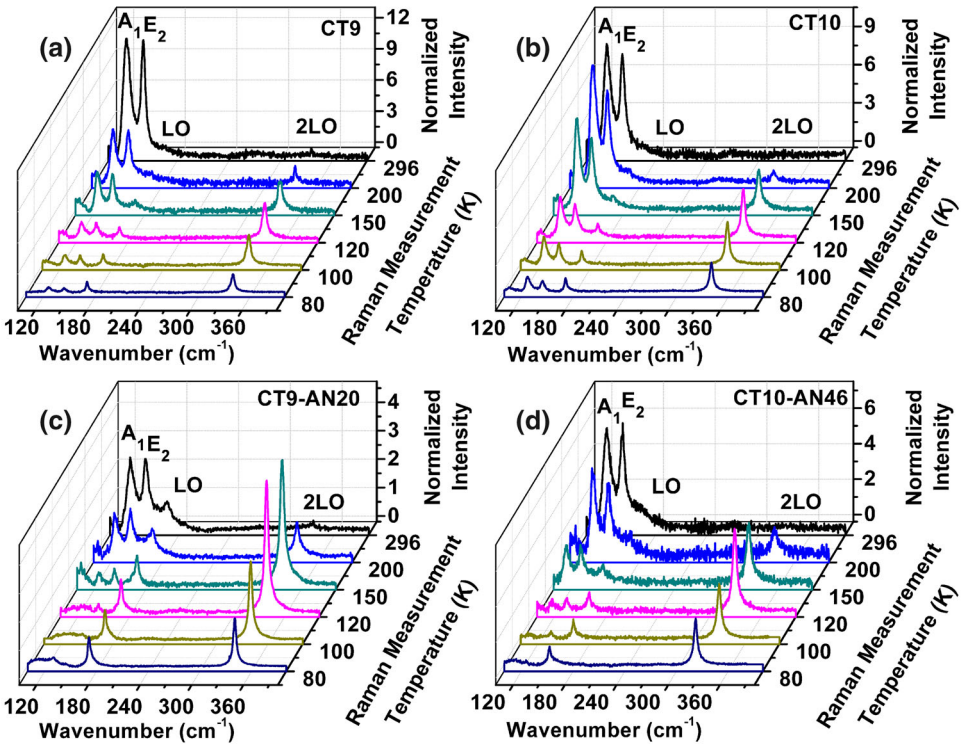

Fig. 4. Raman spectra of (a) as-grown CT9, (b) as-grown CT10, (c) CT9-AN20, and (d) CT10-AN46 samples. Each spectrum for a sample is taken at a different temperature, ranging from 80 K to 296 K.

Table I. Raman intensity ratios of 2LO phonon peaks to LO phonon peaks for various samples measured at temperatures from 80 K to 296 K

	Temperature					
Sample name	**80 K**	**100 K**	**120 K**	**150 K**	**200 K**	**296 K**
CT9	1.78	2.82	3.78	5.23	3.21	1.48
CT10	2.11	3.30	4.95	5.08	0.97	0
CT9-AN20	1.80	3.33	4.05	4.38	1.30	0.18
CT9-AN46	2.89	3.38	5.48	4.56	2.08	0

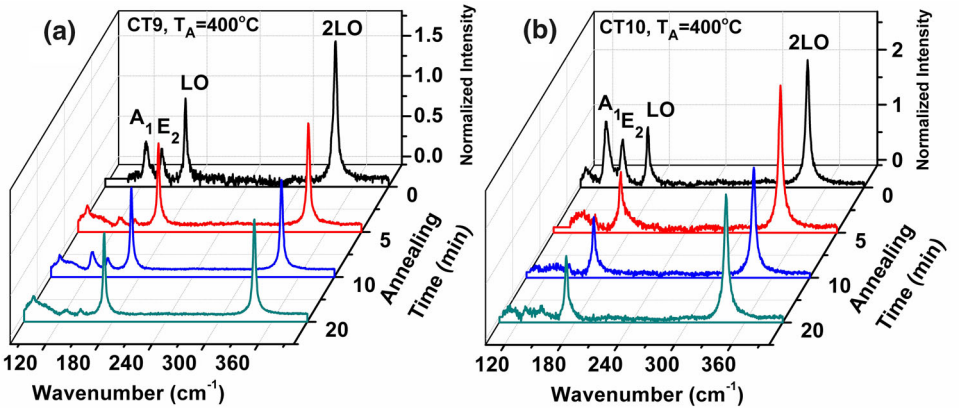

Fig. 5. Raman spectra of (a) CT9 and (b) CT10 samples annealed at 400°C and measured at 80 K as a function of annealing time.

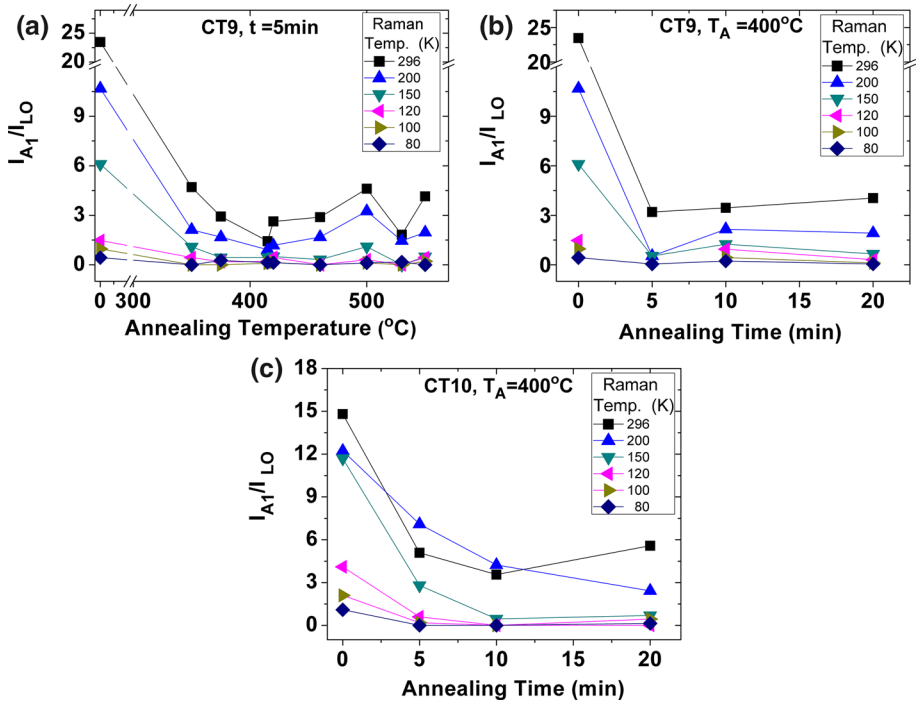

Fig. 6. Intensity ratios of Te A_1 to CdTe LO peaks of (a) as a function of annealing temperature for CT9 for 5 min, (b) as a function of annealing time for CT9 at 400°C, and (c) as a function of annealing time for CT10 at 400°C. Each set of data points represents a specific measurement temperature.

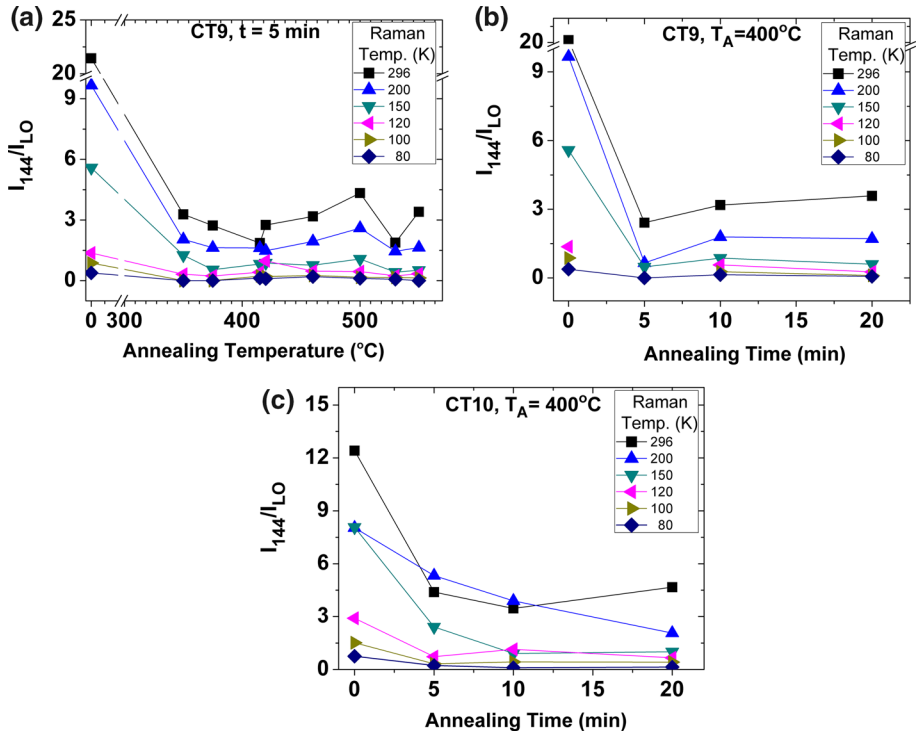

Fig. 7. Intensity ratios for the 144 peak to CdTe LO peaks are given in (a) as a function of annealing temperature for CT9 samples for 5-min annealing duration, in (b) as a function of annealing time for CT9 samples at 400°C annealing temperature, and in (c) as a function of annealing time for CT10 samples annealed at 400°C.

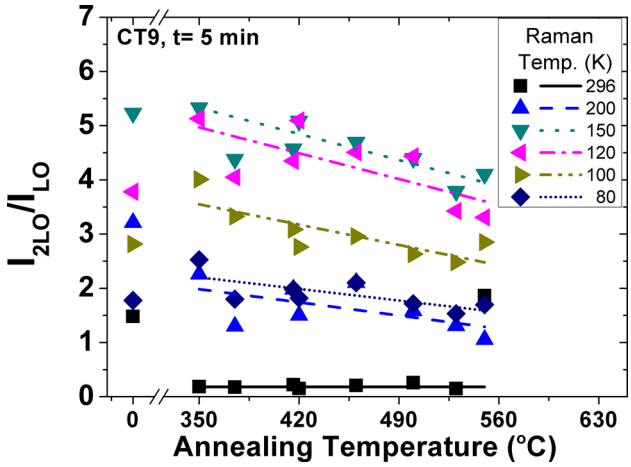

Fig. 8. Intensity ratios of 2LO to LO peaks as a function of annealing temperature for 5-min durations for CT9 samples.

that the smallest I_{2LO}/I_{LO} ratio obtained at 80 K is about 1.5, which was obtained from the sample annealed at 530°C which is fairly close to the value given in the literature (about 1). Thus, we conclude that the best annealing temperature for 5-min annealing duration is about 530°C for a good quality CT9 sample.

Figure 9 shows the I_{2LO}/I_{LO} ratios for CT9 and CT10 samples for varying annealing durations. From Fig. 9a, we can see that I_{2LO}/I_{LO} ratios for varying Raman measurement temperatures decreased exponentially but slowly with annealing duration for CT9 samples annealed at 400°C. In Fig. 9b, we see a similar exponential (asymptotic) decrease in the I_{2LO}/I_{LO} ratios for the CT9 samples annealed at 300°C for the Raman spectra measured from 80 K to 150 K while the spectra measured at 200 K and above exhibit minima for the I_{2LO}/I_{LO} ratios for the annealing durations between 6 h and 12 h. On the other hand, the I_{2LO}/I_{LO} ratios for the CT10 samples decreased linearly but slowly with increasing annealing duration as seen in Fig. 9c. None of the CT10 samples (both as-grown and annealed) exhibit any 2LO peak at 296 K. For any given annealing duration, I_{2LO}/I_{LO} ratios increased with decreasing Raman measurement temperature down to 120 K and decreased with temperature from 120 K to 80 K. As we indicated earlier, the density of phonons increase with temperature, the probability of a photon interacting with two LO phonons also increase up to 150 K and 120 K for the CT9 and CT10 samples, respectively, while, due to increased scattering effects from all phonons, this probability starts to decrease with increasing temperature for higher sample temperatures. The slow and linear reduction of 2LO to LO ratio in CT10 is another indication that these samples have higher Te concentrations than the CT9 samples.

The SEM micrographs of Everson-etched CT9 samples (as-grown and annealed) are given in Fig. 10. The EPD values found from the SEM images are given in Fig. 11. Figure 11a shows the measured EPD values as a function of annealing temperature where the data for 0°C is for no annealing. Each data point was obtained for a sample whose temperature was quickly raised from room temperature to the annealing temperature (by setting the annealing current directly to its final value) and kept steady for the annealing duration. The only exception to this is the data point at 190°C (shown as a diamond symbol) which was obtained from the sample whose temperature was raised to the annealing temperature in 2 min and kept constant for 5 min. As seen from the figure, the lowest EPD values were obtained for the samples annealed at the 400–450°C annealing temperature range for the 5-min annealing duration. Figure 11b displays the EPD values for CT9 samples annealed at 400°C, as a function of annealing time, while in Fig. 11c, the EPD values for the CT9 samples annealed at 420°C are given as a function of the cycle number where the total annealing duration was fixed at 10 min for each sample. Each data point is the average of three data points collected from a different area of the surface of a sample. As seen from Fig. 11b, the EPD values decreased with increasing annealing time. In Fig. 11c, 0 cycle means no annealing while 1 cycle corresponds to one annealing for the whole 10 min. Although the EPD value decreased with increasing cycle number up to 2, then it increased back for 4 cycle annealing. Thus, it seems that 2.5 min annealing time for the 4 cycle case was not enough to reach a minimum in the number of etch pits at 420°C for the CT9 samples. In (a) and (b), theoretical fits to data using Eqs. 7, 8, and 9 are also given as solid curves. We think that in the CT9 samples dislocation coalescence was the dominant process during their annealings, hence Eq. 7 is valid. From the theoretical fit of EPD versus annealing time (Fig. 11b), we found the coefficient K_2 for 700 K, and using this data we adjusted the parameters v_0 and Q to obtain a rough fit for EPD as a function of temperature for the 5-min annealing duration, as seen in Fig. 11a. The initial increase in the EPD value is not explained by the theory given above. We think that, due to the high activation energies of dislocations, their movements require high temperatures, thus initially preventing the coalescence of the dislocations. In the meantime, due to high-temperature stress, the dislocation concentration increases up to 350°C, as seen in Fig. 11a. Then, as the annealing temperature increases, the thermal activation energy barrier is exceeded and the dislocation movement starts, causing the reduction of dislocation densities due to the coalescence process. From the fit in Fig. 11a, we have found the activation energy of the dislocation movement to be 1.2 eV, where v_0 was taken as a free fitting parameter which was about 1 cm/s. We have not carried out any theoretical fit to Fig. 11c since it does not add much information to the discussion of dislocations.

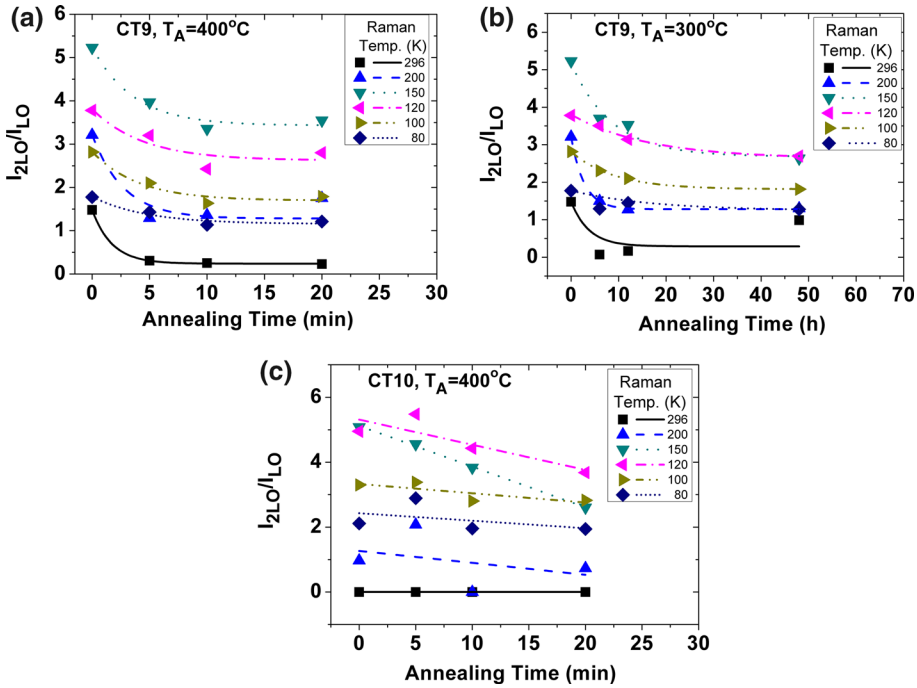

Fig. 9. Intensity ratios of 2LO to LO peak as a function of annealing time (a) at 400°C for CT9, (b) at 300°C for CT9, and (c) at 400°C for CT10 samples.

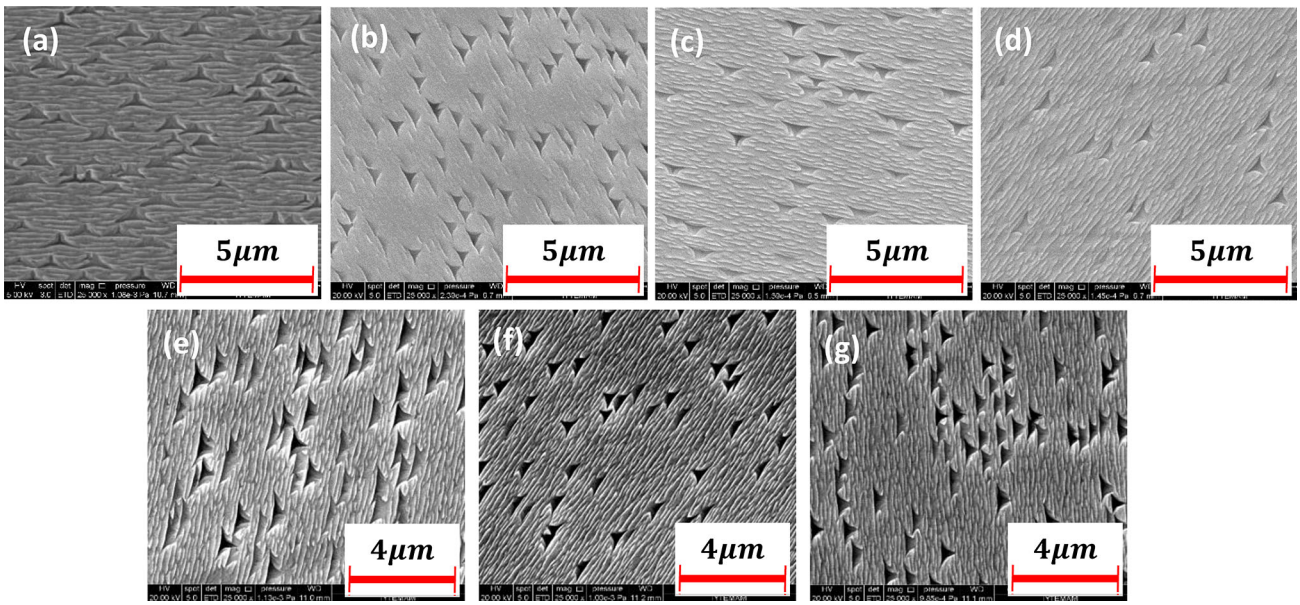

Fig. 10. SEM micrographs of etched samples: (a) CT9-as-grown, (b) CT9-AN6-E (5 min), (c) CT9-AN10-E (10 min), (d) CT9-AN11-E (20 min), (e) CT9-AN32-E (1 cycle, 10 min), (f) CT9-AN33-E (2 cycles, total duration: 10 min), and (g) CT9-AN34-E (4 cycles, total duration: 10 min), where the sample names are given in capital letters and annealing times and cycle numbers are given in parentheses.

In Ref. 17, the activation energy for dislocations in GaAs is given as 1.35 eV, while their velocities are close to 1 cm/s which is in accordance with our results even though the host is different.

Some CT10 samples were also annealed for 5, 10, and 20 min and etched for pit decoration. The SEM micrographs of as-grown and etched CT10 samples are displayed in Fig. 12, and the calculated EPD values from the SEM images are plotted in Fig. 13. As can be seen, the EPD values for CT10 samples increased with increasing annealing time, opposite to the case for the CT9 samples where EPD decreased with annealing duration. The increase in the EPD values for the CT10 samples may be due to the fact that these samples contain more Te precipitations than do the CT9 samples, as seen

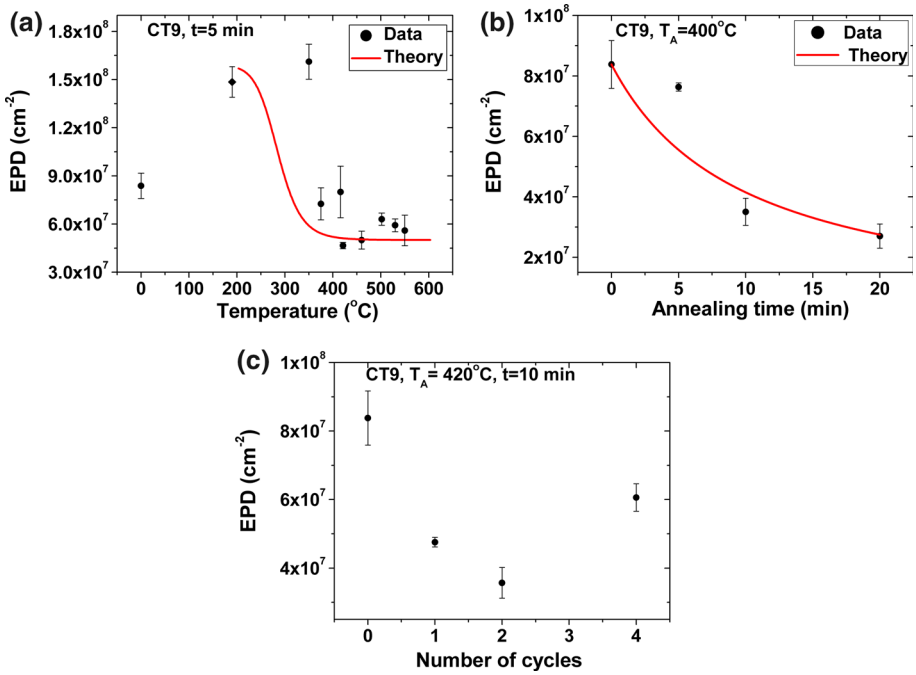

Fig. 11. Etch pit density (EPD) values for some CT9 samples (a) as a function of annealing temperature, (b) as a function of time, and (c) as a function of annealing cycle. Theoretical fit to data is also given in (a) and (b).

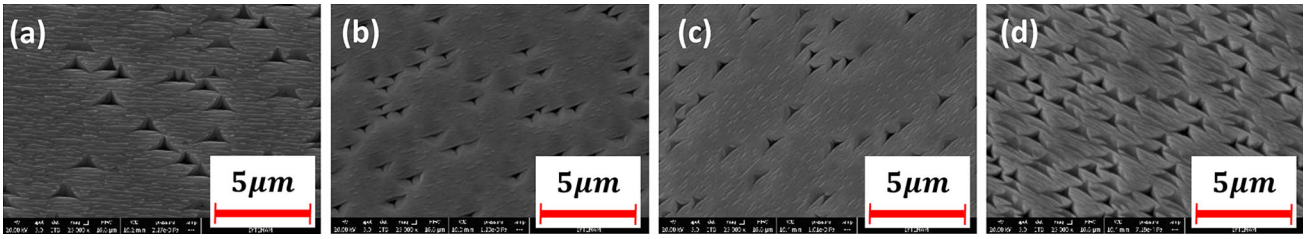

Fig. 12. SEM micrographs of etched (a) CT10-As grown-E, (b) CT10-AN46-E, (c) CT10-AN47-E, and (d) CT10-AN48-E.

from their Raman spectra in Figs. 5, 6c, and 7c and the XRD spectra of the CT9 and CT10 as-grown wafers. Hence, as the annealing duration was increased for the CT10 samples, the number and size of the Te precipitates decreased, causing an increase in the number of dislocations in their places which were seen as increased EPD values for the etched CT10 samples.[45] Although the decreased Te precipitate amounts increased the EPD values for the CT10 samples, we cannot say that the opposite was true for the CT9 samples, namely the decreased EPD values in the CT9 samples do not necessarily mean increased amounts of Te precipitates in them, since we can safely claim that Te precipitates will only form during the growth but not during the annealing, since annealing temperatures are too low to change the stoichiometry of CdTe whose melting temperature is 1092°C at

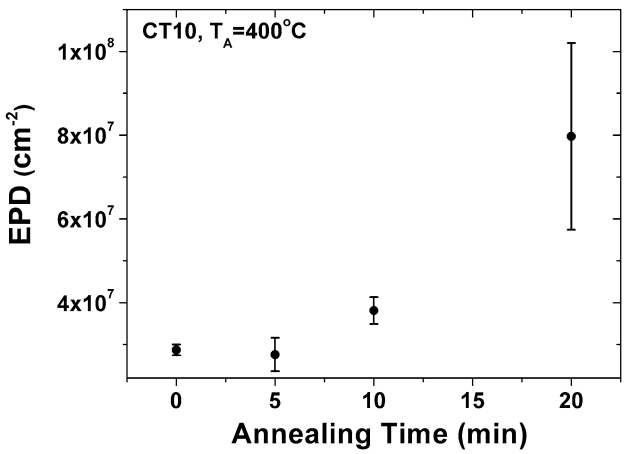

Fig. 13. Etch pit density values for CT10 samples as a function of annealing time.

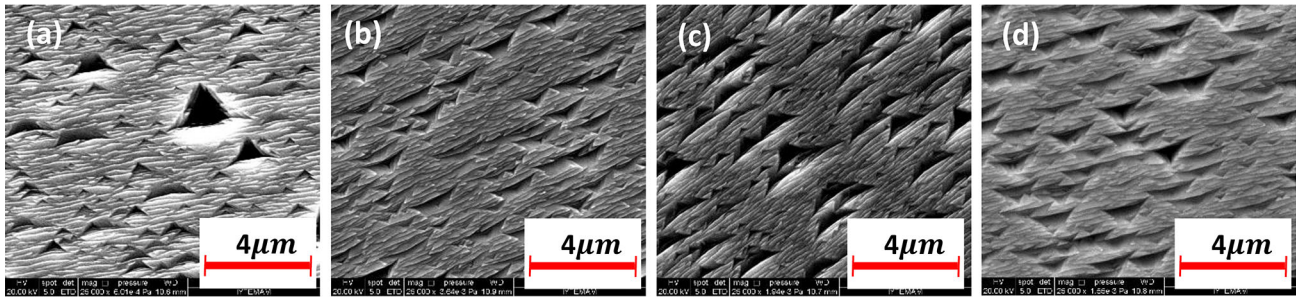

Fig. 14. SEM micrographs of etched samples for (a) 1 cycle, (b) 2 cycles, (c) 3 cycles, and (d) 4 cycles.

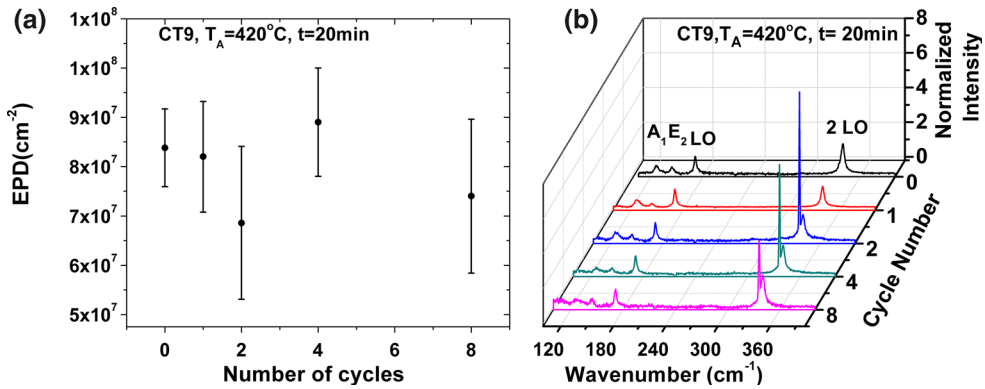

Fig. 15. (a) Etch pit density values for cycle annealed CT9 samples annealed at 420°C and (b) Raman spectra of the same samples, measured at 80 K, plotted as a function of cycle number.

1 atm pressure.[46] On the other hand, an annealing process can cause an increase in the Te precipitate amounts only when the annealing is carried out under Te overpressure, as reported by Refs. 47 and 48. Since our annealings were carried out in vacuum with no extra Te source to create Te overpressure, it is safe to say that there were no increased Te precipitate amounts in any of our samples.

We also carried out cycle annealings for another group of CT9 samples where we fixed the total annealing time at 20 min (as opposed to the earlier 10-min annealing case) while keeping the annealing temperature at 420°C. Figure 14 shows the SEM images of these samples annealed for (a) 1 cycle, (b) 2 cycles, (c) 4 cycles, and (d) 8 cycles. Compared to the 10-min annealed samples where the pit sizes are more or less the same, as seen in Fig. 10e–g, Fig. 14 shows clearly that the etch pit sizes in the 20-min annealed samples are usually smaller than those of the 10-min annealed samples with only a few exceptionally large ones (here, 20 and 10 min are total annealing times). The EPD values, however, do not show a constant decrease with annealing cycle, as was the case for the 10-min annealed samples, but vary between 5×10^7 pits/cm^{-2} and 1.0×10^8 pits/cm^{-2}, as seen in Fig. 15a. Here, we see that longer annealing times at 420°C increase the number of defects up to values for the as-grown samples. This indicates that the re-emission of dislocations becomes important for longer durations and increased numbers of cycles.[18]

Figure 15b shows the Raman spectra of 20-min annealed CT9 samples with different annealing cycle numbers. We see an additional sharp and intense peak centered at 336 cm^{-1} which was not observed in the Raman spectra of other samples. This peak is possibly due to an electronic transition since it does not show a considerable shift with temperature and its full width at half maximum value is much smaller than those of other peaks. It might be due to some defect structure which occurred at longer annealing durations such as a host vacancy or some foreign atom (possibly an oxygen atom) near or on the surface of our CdTe films. The second possibility is more probable since this peak disappeared when the laser shone on the sample for some time, indicating the breaking of the bonds with the host.

CONCLUSION

In this work, we studied the structural and surface defects of MBE-grown CdTe films by an etch pit analysis employing SEM micrography along with Raman and XRD spectroscopies. The cycle

annealing of the CT9 samples at 420°C clearly displayed a decrease in the EPD values of the 10-min annealed samples while the 20-min annealed CT9 samples showed varying etch pit sizes with more or less the same EPD values as those for the 10-min samples. The EPD values decreased with annealing time for the CT9 samples; however, they increased for the CT10 samples when the annealing temperature was kept at 400°C for both sample groups. We interpreted this as indicating that the increased EPD values in the CT10 samples were due to a reduction in the amount of Te precipitates during annealing, since these samples contained more Te precipitates than the CT9 samples.

In fact, for all annealings of both the CT9 and CT10 samples, we observed a clear reduction in the amount of Te precipitates which was also confirmed from the Raman spectra of these samples, where the phonon peaks of the Te precipitates became smaller or sometimes disappeared with annealing. We have seen that Raman measurements taken at high temperatures give a better understanding of Te peaks which are more pronounced at room temperature. To judge the quality of the samples, we considered the intensity ratios of CdTe 2LO to CdTe LO peaks in their Raman spectra taken at 80 K, which should be near unity according to the literature. For the CT10 samples, this ratio remained at about 2, while for the CT9 samples it decreased from 2.5 to 1.0 with the increasing annealing temperature and time. In that sense, the best quality sample, when compared with the literature, was a CT9 sample annealed for 20 min at 400°C.

Theoretical fits for the EPD values as a function of time and temperature gave the activation energy of movements of dislocations and their velocities as 1.2 eV and 1 cm/s, respectively, which are close to those reported in the literature for bulk GaAs samples. Hence, we can say that the dislocation movements in CdTe are similar to those in GaAs.

This work provides an insight into understanding and reducing the structural and surface defects in MBE-grown thin films of CdTe grown on GaAs wafers. This structure is important for technological applications especially for their use in detector technologies and solar cell applications.

ACKNOWLEDGEMENTS

We would like to thank Elif Bilgilisoy for her help in the etching of samples and Mustafa Polat for XRD measurements. We appreciate Dr. George Petterson for his help and contribution in the MBE growth of the samples. We also would like to thank Dr. John Reno for his interpretations and comments on our MBE-grown samples. Finally, we are grateful to SSM (Undersecretariat for Defence Industries of Turkey) and ASELSAN as their financial support.

FUNDING

This study was funded by ASELSAN ('GEDİZ' Project).

REFERENCES

1. C. Verie, *Festkörper Probleme X Advances in Solid State Physics*, 1st ed. (Oxford: Pergamon, 1970).
2. W.M. Higgins, G.N. Pultz, R.G. Roy, R.A. Lancaster, and J.L. Schmit, *J. Vac. Sci. Technol. A* 7, 271 (1989). https://doi.org/10.1116/1.576110.
3. J. Welser, J.L. Hoyt, and J.F. Gibbons, *IEEE Electron. Device Lett.* 15, 100 (1994).
4. M.A. Kinch, *J. Electron. Mater.* 44, 2969 (2015). https://doi.org/10.1007/s11664-015-3717-5.
5. J.D. Benson, L.O. Bubulac, P.J. Smith, R.N. Jacobs, J.K. Markunas, M. Jaime-Vasquez, L.A. Almeida, A. Stoltz, J.M. Arias, G. Brill, Y. Chen, P.S. Wijewarnasuriya, S. Farrell, and U. Lee, *J. Electron. Mater.* 41, 2971 (2012). https://doi.org/10.1007/s11664-012-2089-3.
6. L. He, X. Fu, Q. Wei, W. Wang, L. Chen, Y. Wu, X. Hu, J. Yang, Q. Zhang, R. Ding, X. Chen, and W. Lu, *J. Electron. Mater.* 37, 1189 (2008). https://doi.org/10.1007/s11664-008-0441-4.
7. M. Reddy, D.D. Lofgreen, K.A. Jones, J.M. Peterson, W.A. Radford, J.D. Benson, and S.M. Johnson, *J. Electron. Mater.* 42, 3114 (2013). https://doi.org/10.1007/s11664-013-2660-6.
8. Y. Chang, C.H. Grein, J. Zhao, and S. Sivanathan, *J. Appl. Phys.* 100, 114316 (2006). https://doi.org/10.1063/1.2399890.
9. S.M. Johnson, D.R. Rhiger, J.P. Rosbeck, J.M. Peterson, S.M. Taylor, and M.E. Boyd, *J. Vac. Sci. Technol. B* 10, 1499 (1992). https://doi.org/10.1116/1.586278.
10. J. Wenisch, D. Eich, H. Lutz, T. Schallenberg, R. Wollrab, and J. Ziegler, *J. Electron. Mater.* 41, 2828 (2012). https://doi.org/10.1007/s11664-012-2113-7.
11. P. Capper, A. Noda, H. Kurita, R. Hirano, S. Adachi, J. Garland, R. Sporken, C.D. Maxey, M. Martyniuk, J.M. Dell, L. Faraone, J. Chu, Y. Chang, D. Shaw, M.A. Berding, C.R. Becker, S. Krishnamurthy, R.J. Westerhout, R.H. Sewell, C.A. Musca, A.J. Stoltz, I.M. Baker, C. Jones, N. Gordon, I. Baker, M. Kinch, J. Piotrowski, A. Piotrowski, *Mercury Cadmium Telluride Growth, Properties and Applications*, 1st ed. (Chichester: John Wiley & Sons, 2011).
12. Y. Chen, S. Farrell, G. Brill, P. Wijewarnasuriya, and N. Dhar, *J. Cryst. Growth* 310, 5303 (2008). https://doi.org/10.1016/j.jcrysgro.2008.09.023.
13. G. Brill, S. Farrell, Y.P. Chen, P.S. Wijewarnasuriya, M.V. Rao, J.D. Benson, and N. Dhar, *J. Electron. Mater.* 39, 967 (2010). https://doi.org/10.1007/s11664-010-1142-3.
14. J.D. Benson, S. Farrell, G. Brill, Y. Chen, P.S. Wijewarnasuriya, L.O. Bubulac, P.J. Smith, R.N. Jacobs, J.K. Markunas, M. Jaime-Vasquez, L.A. Almeida, A. Stoltz, U. Lee, M.F. Vilela, J. Peterson, S.M. Johnson, D.D. Lofgreen, D. Rhiger, E.A. Patten, and P.M. Goetz, *J. Electron. Mater.* 40, 1847 (2011). https://doi.org/10.1007/s11664-011-1670-5.
15. S. Farrell, M.V. Rao, G. Brill, Y. Chen, P. Wijewarnasuriya, N. Dhar, D. Benson, and K. Harris, *J. Electron. Mater.* 40, 1727 (2011). https://doi.org/10.1007/s11664-011-1669-y.
16. S. Simingalam, G. Brill, P. Wijewarnasuriya, and M.V. Rao, *J. Electron. Mater.* 44, 1321 (2014). https://doi.org/10.1007/s11664-014-3542-2.
17. M. Yamaguchi, A. Yamamoto, M. Tachikawa, Y. Itoh, and M. Sugo, *Appl. Phys. Lett.* 53, 2293 (1988). https://doi.org/10.1063/1.100257.
18. M. Yamaguchi, M. Tachikawa, Y. Itoh, M. Sugo, and S. Kondo, *J. Appl. Phys.* 68, 4518 (1990). https://doi.org/10.1063/1.346156.
19. W.J. Everson, C.K. Ard, J.L. Sepich, B.E. Dean, G.T. Neugebauer, and H.F. Schaake, *J. Electron. Mater.* 24, 505 (1995).
20. C.V. Raman, *Ind. J. Phys.* 2, 387 (1928).

21. A. Mooradian and G.B. Wright, in *Proceedings of the Ninth International Conference on the Physics of Semiconductors, Moscow, 1968* (Nauka, Leningrad, 1968), p 1020.
22. S. Perkowitz, *Optical Characterization of Semiconductors: Infrared, Raman, and Photoluminescence Spectroscop* (Atlanta: Academic Press, 1993).
23. S.H. Shin, J. Bajaj, L.A. Moudy, and D.T. Cheung, *Appl. Phys. Lett.* 43, 68 (1983). https://doi.org/10.1063/1.94123.
24. P.M. Amirtharaj and F.H. Pollak, *Appl. Phys. Lett.* 45, 789 (1984). https://doi.org/10.1063/1.95367.
25. D.J. Williams and A.W. Vere, *J. Vac. Sci. Technol. A* 4, 2184 (1986).
26. N.G. Chew, A.G. Cullis, and G.M. Williams, *Appl. Phys. Lett.* 45, 1090 (1984).
27. Z.C. Feng, S. Perkowitz, J.M. Wrobel, and J.J. Dubowski, *Phys. Rev. B* 39, 1299 (1989).
28. J.R.M. Contreras, C.F. Reyes, C.I.M. Ruiz, H.P.L.D. Guevara, and C.M. Gutierrez, *J. Phys. D Appl. Phys.* 46, 245105 (2013). https://doi.org/10.1088/0022-3727/46/24/245105.
29. Veeco MBE Systems, C.D., St. Paul, MN 55127.
30. AXT Company, T.D., Fremont, CA 94538, USA.
31. L. Van Laake, A.J. Hart, and A.H. Slocum, *Rev. Sci. Instrum.* 78, 083901 (2007). https://doi.org/10.1063/1.2760936.
32. S&I Spectroscopy and Imaging GmbH, Warstein, Germany.
33. Linkam Scientific Instruments, U.E.D.M.C.W., Tdworth, Surrey, UK.
34. FEI QUANTA 250 FEG, E.M.C., University of Kentucky, Lexington.
35. Q. Li, K. Chi, Y. Mu, W. Zhang, H. Yang, W. Fu, and L. Zhou, *Mater. Lett.* 117, 225 (2014).
36. R.W.G. Wyckoff, *Crystal Structures 1*, 2nd ed. (New York: Interscience Publishers, 1963).
37. W. Richter, J.B. Renucci, and M. Cardona, *Phys. Status Solidi B* 56, 223 (1973).
38. K.J. Mackey, D.R.T. Zahn, P.M.G. Allen, R.H. Williams, W. Richter, and R.S. Williams, *J. Vac. Sci. Technol. B* 5, 1233 (1987). https://doi.org/10.1116/1.583719.
39. A. Lusson, J. Wagner, and M. Ramsteiner, *Appl. Phys. Lett.* 54, 1787 (1989). https://doi.org/10.1063/1.101295.
40. N.V. Sochinskii, M.D. Serrano, E. Dieguez, F. Agullorueda, U. Pal, J. Piqueras, and P. Fernandez, *J. Appl. Phys.* 77, 2806 (1995). https://doi.org/10.1063/1.358687.
41. D. Nam, H. Cheong, A.S. Opanasyuk, P.V. Koval, V.V. Kosyak, and P.M. Fochuk, *Phys. Status Solidi C* 11, 1515 (2014). https://doi.org/10.1002/pssc.201300577.
42. T.A. Germer, N.M. Haegel, and E.E. Haller, *J. Appl. Phys.* 60, 1055 (1986).
43. A.S. Pine and G. Dresselhaus, *Phys. Rev. B* 4, 356 (1971).
44. G.A.N. Connell, R.J. Nemanich, and C.C. Tsai, *Appl. Phys. Lett.* 36, 31 (1980). https://doi.org/10.1063/1.91304.
45. Y. Selamet, *HGCDTE Heterojunctions Grown by MBE for Infrared Detection Applications: An In Situ Doping Approach* (Chicago: University of Illinois at Chicago, 2004).
46. J.W. Rutter and B. Chalmers, *Can. J. Phys.* 31, 15 (1953).
47. M. Ayoub, M.H. Ali, A. Zumbiehl, R. Regal, J.M. Koebel, C. Rit, P. Fougeres, and P. Siffer, *IEEE Trans. Nucl. Sci.* 49, 1954 (2002).
48. K. Yokota, T. Yoshikawa, S. Katayama, S. Ishihara, and I. Kimura, *JJAP* 24, 1672 (1985).